THE JOURNAL OF PHYSICAL CHEMISTRY C

pubs.acs.org/JPCC Article

Roughness Effects on the Surface Charge Properties of Silica Nanoparticles

B. Oyku Alan, Murat Barisik,* and H. Gokberk Ozcelik

Cite This: J. Phys. Chem. C 2020, 124, 7274−7286 Read Online

ACCESS | Metrics & More | Article Recommendations

ABSTRACT: The surface charge property of silica nanoparticles plays a key role in their function. Previous studies assumed surface charge as a homogeneously distributed constant material property, independent of the nanoparticle size and surface condition. Instead, this study considered surface chemistry as a function of local ionic conditions (Charge Regulation) to calculate the local surface charges around a rough nanoparticle, as an extension to our earlier study (*J. Phys. Chem. C* **2014,** *118* (4), 1836−1842). For the current surface heterogeneity in the form of concave and convex circles, the surface charge showed a distinct local variation: decrease due to the electrical double layer (EDL) overlap in the valleys and increase due to curvature effects on the hills of the surface structure. The average of local surface charges decreased with the decrease of the roughness size (D_R), depending on the particle size (D_P) and pH. We characterized the variation of the average surface charge by a nondimensional group we formed as a measure for the EDL overlap and curvature effects $[(D_R/\lambda) \times (D_R/D_P)]$. Based on this, we devised a phenomenological model as an extension to the existing flat surface theory, which can successfully predict the average surface charge around a rough/patterned nanoparticle as a function of the particle size, roughness size, and pH.

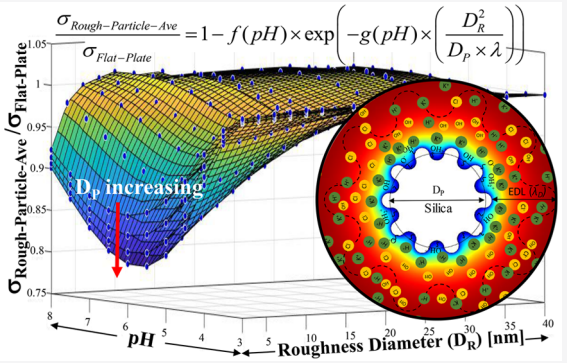

INTRODUCTION

In recent years, silica nanoparticles (SNPs) have become one of the most popular nanomaterials because of their unique physical and structural properties such as high surface areas, tunable particle sizes and surface conditions, high in vivo and in vitro compatibilities, and high colloidal stability. Hence, SNPs became a promising tool for biomedical applications such as bioimaging for diagnostics,[1,2] biosensing,[3] biocatalysis,[4,5] drug delivery,[6−8] gene delivery,[9−11] and anticancer therapeutic agents.[12] In all these applications, the surface electric charge of SNPs plays a key role, but a complete characterization in terms of SNP properties is missing.

SNPs are great candidates for drug-delivery applications. For example, SNPs can be designed to accumulate in tumors by passive targeting via enhanced permeability and retention effects or by active targeting via covering the surface with specific cancer cell-targeting molecules. SNPs need to be designed to (i) enter only the targeted type of cell, (ii) carry the required amount of drug, (iii) remain inside the cell long enough to release the required drug without being destroyed, and (iv) maintain their properties close to the designed conditions. Such a specific nanocarrier can be obtained by adjusting the size, morphology, and surface conditions but, more importantly, by calibrating the electrokinetic properties of the SNP. The importance of electric charge of the SNP can be explained through some of the major mechanisms of the above listed four steps of targeted drug delivery. First, drug loading-releasing mechanisms depend on the surface charge.[13] Effective and selective loading of drugs as well as the targeted and sustained drug release were shown to be controlled by tailoring the surface charge properties of SNPs.[14−16] Second, cellular uptake is determined by the surface charge. Studies reported that 100−150 nm nanoparticles were more efficient for cellular uptake compared to 50−55 nm SNPs.[17,18] The underlying mechanisms are described by the variation of the surface charge by the nanoparticle size; a decrease in the nanoparticle diameter increases the absolute charge value.[19] Third, endosomal escape was found to be strongly dependent on the surface charge. The entrapment in the endosomes may lead to disruption of nanocarriers and drugs by digestive enzymes that endosomal escape is very important for the efficient delivery of the nanoparticles.[20] Studies reported that SNPs with negatively charged surface properties achieve endosomal escape easier.[21] Fourth, protein corona formation

Received: January 6, 2020
Revised: February 14, 2020
Published: February 28, 2020

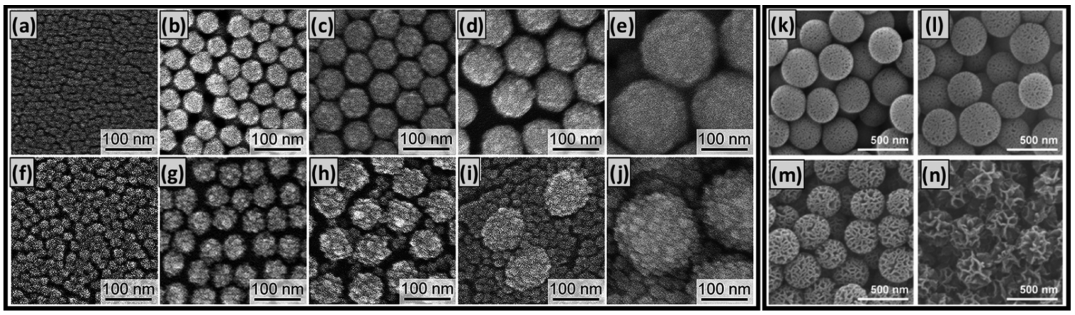

Figure 1. (a–j) Different size [(a & f) 12, (b & g) 44, (c & h) 60, (d & i) 88, and (e & j) 170 nm] SNPs with flat (a–e) and rough (f–j) surface conditions developed by Koike et al.[24] and published by The Royal Society of Chemistry. (k–n) Various surface conditions of wrinkled SNPs obtained by Kang et al.[25] and published by The Nature Publishing Group.

on the nanoparticles by the coverage of biomolecules (such as proteins, sugars, and lipids) is directly related to the surface charge.[22] Protein corona has a dynamic structure, and it defines the identity of the nanoparticle.[23] The presence of a protein corona modifies the surface properties and changes the hydrodynamic diameter and electrokinetic properties of the nanoparticle. Considering all these facts, it is crucial to characterize the surface electric properties of SNPs.

When a nanoparticle is immersed in an aqueous medium, the association/disassociation reactions on the surface and the adsorption of ions yield a surface charge as a function of the electrolyte concentration and pH. The charged nanoparticle surface attracts counterions and repels coions, and an ionic layer described as the electrical double layer (EDL) will be formed on the surface. The electric charge of the surface can be calculated analytically for an ideal system by assuming that the ionic distribution on the surface is described by the Boltzmann distribution. However, such an assumption is only valid for zeta potentials smaller than 25 mV and for flat surfaces with no curvature and no overlapping EDLs. Much of the literature employs the classical Poisson–Boltzmann (PB) solutions to calculate the surface zeta potential for nanosystems as a constant property of the corresponding material. For SNPs, these assumptions are invalid; simply, the particle surface is curved, and surface structures develop overlapping EDLs. With the help of recent techniques, various forms of SNPs with different particle sizes and surface conditions have been synthesized. For instance, different particle sizes under two different surface conditions are presented in the study of Koike et al.[24] (Figure 1a–j), and different surface conditions at a given particle size are shown in the study by Kang et al.[25] (Figure 1k–n). For such nanosystems, the particle size and surface condition determine the local variation of the ionic concentration and the resulted zeta potential on the surface. First, a decrease in the overall particle size develops curvature effects that the ionic condition around the particle diverges from a flat surface. Curvature effects are due to the decreased surface-to-volume ratio due to the decrease in the particle diameter as observed through several studies.[19,26,27] Second, the surface structures of either naturally developed or engineered surface patterns/roughness create local variation of ionic distribution, which differs from the existing flat surface theory. In the case of nanoparticle roughness composed of valleys and hills, ionic layers in the valleys extending from opposing convex surfaces overlap, whereas curvature effects develop over the concave surfaces at the hills of the surface roughness. Such a local variation of electric charge as a function of the surface nanotopology was observed by a few studies through atomic force microscopy (AFM) measurements[28] and numerical simulations[29,30] over planar surfaces, but it has never been studied for nanoparticles, yet.

Understanding the relation between the surface charge of an SNP and its structural parameters, such as the particle size and surface condition, will be useful to calculate the correct average surface charge for a given SNP. At the same time, such knowledge will also be useful for so-called "surface charge patterning at nanoscale" practices, where a nonhomogenous surface charge distribution is exercised to control the thermodynamic phase behavior of colloids,[31,32] design the behavior of nanoparticles,[33,34] and develop desired Janus particles.[35] However, modification of the surface charge distribution is frequently done using very sophisticated and complicated techniques such as positioning charges using AFM[36] and optical tweezers[37] or controlling the self-assembly of biological/chemical groups[38] and nanoparticles.[39] Instead, the manipulation of the local surface charge can be obtained by simply changing the surface topography. Because surface patterning is employed by larger communities, the fabrication techniques are more established. Manipulation of the surface charge by changing the surface topography was utilized recently by creating fractal structures as an electrode for enhanced electrophoresis properties[40] and efficiency in detecting biomolecules.[41]owever, there is no proper correlation between the surface topography and surface charge of the nanoparticles. Understanding of local surface charge variation will also be important for dielectrophoresis-based electrokinetic applications.[42−44]

In order to properly calculate the nanoparticle surface charge, first, ionic diffusion must be defined by Poisson–Nernst–Planck (PNP) equations without Boltzmann assumption.[45,46] Next, rather than defining a constant surface charge/potential boundary condition, the electrical charge on the surface should be calculated as a function of the ionic density forming on the surface. In such a case, the development of surface charge and the resulting EDL are coupled;[47,48] also called "Charge Regulation (CR)," this physicochemical nature of surfaces was first identified by Ninham and Parsegian[49] and later observed by multiple experiments in surface force measurements using colloids[50,51] and AFM.[52,53] Since then, researchers have attempted to apply CR into calculations by using active charge models as boundary conditions to resolve the surface charging of silica nanochannels,[48,54−57] nanopores,[58−61] mesoporous systems,[62,63] and nanoparticles.[19,64,65] Using this systematic approach, we characterized the surface charging of SNPs for the case of flat surface condition without any roughness.[19] For the first time in the literature, we

https://dx.doi.org/10.1021/acs.jpcc.0c00120
J. Phys. Chem. C 2020, 124, 7274−7286

presented that the SNP surface charge depends on the nanoparticle size.[19] Just recently, we studied the charge of planar surfaces with varying sizes of surface nanopatterns/roughness.[66] Although lower and higher charges were observed at the pits and tips of the surface pattern, the average of local surface charges became lower than the theoretical predictions. Based on the numerical calculations, a phenomenological model was developed as an extension to the existing flat surface theory to predict the average surface charge on a nanopatterned surface as a function of the surface pattern size, ionic concentration, and pH.

The aim of this work is to extend our earlier experience toward investigation of the effects of surface roughness on SNP surface charging for the first time in the literature. We will study different size SNPs at various surface roughness and pH values. For a constant nanoparticle size, variation of surface structural conditions, which is classically identified as variation of the surface area, is intended to be represented by the change in the size of self-repeating circular surface structures around the nanoparticle.

THEORETICAL AND COMPUTATIONAL DETAILS

A SNP surface with circular nanostructures with diameter D_R is illustrated in Figure 2. The representative nanoroughness/pattern in the form of repeating concave and convex circles was formed as a function of the roughness diameter D_R. Such a form of surface pattern enables us to control the surface structures by simply varying the single quantity, D_R, and perform a parametric study by systematically varying it. Furthermore, the charging mechanisms developing on the circular pattern are similar to the flat surface nanoparticles we previously studied[66] and can be validated with our earlier work.

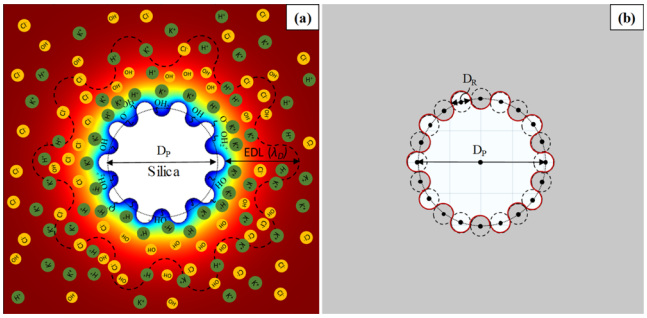

Figure 2. (a) Schematic illustration of the simulation domain consisting of a patterned silica surface and four different ionic species with natural silanol groups of the silica surface. (b) Description of the surface heterogeneity in the form of the simple circular geometric model.

The liquid phase is a KCl aqueous electrolyte solution consisting of four types of ionic species, namely, H^+, K^+, Cl^-, and OH^- ions, with their bulk values as c_{10}, c_{20}, c_{30}, and c_{40}, respectively. Bulk concentration of the ionic species is defined as[58,67−69]

$$c_{10} = 10^{-\mathrm{pH}+3} \qquad c_{40} = 10^{-(14-\mathrm{pH})+3} \tag{1}$$

$$c_{20} = c_{\mathrm{KCl}} \qquad c_{30} = c_{\mathrm{KCl}} + c_{10} - c_{40} \text{ for pH} < 7 \tag{2}$$

$$c_{20} = c_{\mathrm{KCl}} + c_{10} - c_{40} \qquad c_{30} = c_{\mathrm{KCl}} \text{ for pH} > 7 \tag{3}$$

The electric potential distribution within the EDL obeys the Poisson equation that is presented in eq 4. In this equation, ε_0 and ε_r are the permittivity of the vacuum and dielectric constant of the aqueous solution, respectively. It should be noted that the dielectric constant may vary depending on the electric potential distribution in the nanochannel, but this effect may be neglected compared to the other variations in the current system. ψ is the electric potential; F is the space charge density; z_i, and c_i are the valence and molar concentration of the ith ionic species (i = 1 for H^+; i = 2 for K^+; i = 3 for Cl^-; i = 4 for OH^-), respectively.

$$-\varepsilon_0\varepsilon_r\nabla^2\psi = F(z_i c_i) \tag{4}$$

The extension of the EDL from the surface is characterized by the Debye length (λ). Debye length can be evaluated by using eq 5. Boltzmann and Avogadro constants are denoted by k_B and N_A, respectively, T is the temperature, and e is the elementary charge.

$$\lambda = \frac{1}{\kappa} = \sqrt{\frac{\varepsilon_0\varepsilon_r k_B T}{N_A e^2 \sum c_i z_i^2}} \tag{5}$$

Transport of ionic mass is governed by the Nernst−Planck equation as shown in eq 6. Here, $\vec{N}_i$ is the flux density, D_i is the diffusivity, and R and T are the universal gas constant and temperature, respectively. Concentrations of ionic species are maintained at their bulk values (i.e., $c_i = c_{i0}$) at far ends of the nanochannel, and no flux of ionic species is allowed through the nanochannel walls.

$$\nabla\cdot\vec{N}_i = \nabla\cdot\left(-D_i\nabla c_i - z_i\frac{D_i}{RT}Fc_i\nabla\psi\right) = 0 \tag{6}$$

The surface reactions develop based on the local ionic environment at the interface that neither the surface charge nor the potential remains constant; instead, both of them undergo variation in response to the variation in ionic distribution and create a new equilibrium accordingly. Such behavior is modelled by the previously developed multi-ion CR model,[19,64] which considers the effects of the protonation/deprotonation surface reactions, the site density of the functional groups, and pH and salt concentration of the aqueous solution on the silica surface. Because of protonation/deprotonation of ions, the silica surface is charged when in contact with an ionic solution. The surface charge is mainly controlled by the K^+ and Cl^- ions, whereas the pH of the solution is adjusted by the H^+ and OH^- ions. Two fundamental dissociation/association reactions are considered at the solid/liquid interface as follows

$$\mathrm{SiOH} \leftrightarrow \mathrm{SiO^-} + \mathrm{H^+} \tag{7}$$

$$\mathrm{SiOH} + \mathrm{H^+} \leftrightarrow \mathrm{SiOH_2^+} \tag{8}$$

The equilibrium constants are evaluated by using

$$K_A = \frac{\Gamma_{\mathrm{SiO^-}}[\mathrm{H^+}]_w}{\Gamma_{\mathrm{SiOH}}}, \qquad K_B = \frac{\Gamma_{\mathrm{SiOH_2^+}}}{\Gamma_{\mathrm{SiOH}}[\mathrm{H^+}]_w} \tag{9}$$

where Γ_{SiO^-}, Γ_{SiOH}, and $\Gamma_{SiOH_2^+}$ are the surface site densities of SiO^-, SiOH, and $SiOH_2^+$, respectively, and $[H^+]_w$ is the hydrogen concentration at the solid/liquid interface. In this regard, the surface charge density of the silica walls can be denoted as

$$\sigma_w = -\frac{F\Gamma_{\mathrm{total}}}{N_A}\frac{K_A - K_B[\mathrm{H^+}]_w^2}{K_A + [\mathrm{H^+}]_w + K_B[\mathrm{H^+}]_w^2} \tag{10}$$

https://dx.doi.org/10.1021/acs.jpcc.0c00120
J. Phys. Chem. C 2020, 124, 7274−7286

Equation 5 basically determines the difference in the number of charged sites (SiO^- and $SiOH_2^+$) at the final equilibrium of the dissociation/association reaction developing on the surface under the corresponding ionic conditions. Similar 2-pK models for dissociation and association reactions have been implemented in the literature for many years because of their success in capturing the titration behavior of an aqueous silica surface.[70] Later, direct measurements of such charging sites were conducted. One of the very first confirmations of surface groups at the silica water interface was done by investigating the oxidation states of surface atoms via X-ray photoelectron spectroscopy (XPS) measurements.[71] Both O 1s spectra[71] and Si 2p spectra[72] from silica XPS measurements exhibit pH-dependent behavior in the electron binding energy. Moreover, increasing the surface charges by increasing the pH described by the CR model was also validated by these experiments. We should also underline here that the current model neglects the Stern layer. Studies have shown that the Stern layer has an important effect on electro osmotic flow,[57] streaming current,[73] and ionic conductance.[74] They mentioned that the Stern layer effect is significant for the pH range of 8−10, but for high pH values, it seems it has nearly no effect on the surface charge.[75]

PNP equations in 2D cartesian coordinates are numerically solved by the finite element method with COMSOL Multiphysics. After a mesh independency study, a fine structured mesh was found to be required within and at the inlet/outlet vicinity of the channel, whereas a coarser triangular mesh structure was adequate for the rest of the domain. The constants and parameters used in the simulations were taken as $\varepsilon_0\varepsilon_r$ = 7.08 × 10^{-10} F/m (the permittivity of vacuum and dielectric constant of the aqueous solution), R = 8.31 J/(mol·K) (the universal gas constant), F = 96485 C/mol (the Faraday constant), T = 300 K (temperature), Γ_{total} = 4.816 #/nm^2[76] (the total surface site density), $pK_A = -\log K_A = 7$, and $pK_B = -\log K_B = 1.9$.[74] Moreover, the diffusivities of H^+, K^+, Cl^-, and OH^- ions are set to be 9.31 × 10^{-9}, 1.957 × 10^{-9}, 2.032 × 10^{-9}, and 5.3 × 10^{-9} m^2/s, respectively.[77]

The numerical model is validated by comparing the results with the experimental measurements of Brown et al.[78] for a 9 nm flat SNP with negligible surface roughness immersed in 50 mM KCl solution. Figure 3 presents the surface charge density values for the pH range from 3 to 8. Numerical results for a flat nanoparticle show good agreement with the experimental data.

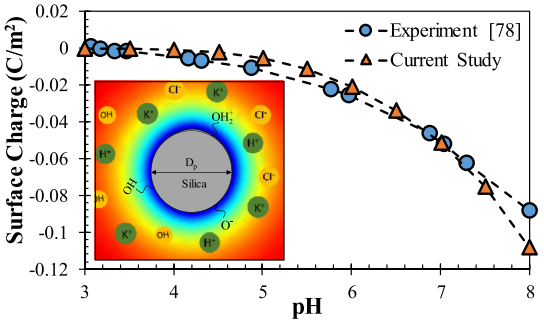

Figure 3. Comparison between numerical results and experimental data of Brown et al.[78] for a 9 nm flat SNP in 50 mM KCl solution. Corresponding simulations were performed using D_P = 9 nm, C_{KCl} = 50 mM, Γ_{total} = 4.75 #/nm^2, $pK_A = -\log K_A = 7$, and $pK_B = -\log K_B$ = 1.9.

RESULTS AND DISCUSSION

Our investigations began by calculating the ionic distribution around the 40, 60, and 100 nm diameter (D_P) nanoparticles with surface roughness diameters (D_R) of 2, 4, and 10 nm at C_{KCl} = 1 mM ionic concentration and pH = 7. Figure 4 presents the electric potential contours of all these cases; each row is at the same roughness diameter, and each column is at the same particle diameter. From bottom to top, when the roughness diameter decreases, the gap between the roughness structures becomes smaller than the EDL thickness. As a result, EDLs extending from the opposite surfaces overlap, and ionic distribution shows local variation along the patterned surface. Interestingly, potential contours around the particle are almost perfectly circular, despite the patterned surface. In contrast, when the roughness diameter is bigger than the EDL thickness, the overlap is diminished and the EDL grows directly from the circular path of surface roughness that the potential contours around the particle show the shape of the surface pattern. Next, from right to left, when the particle diameter decreases, the EDL thickness over the particle increases because of curvature effects. As a result of local variation of ionic distribution, surface electric properties also develop local variation described by the CR nature of surface physicochemistry, calculated by the active electric boundary condition.

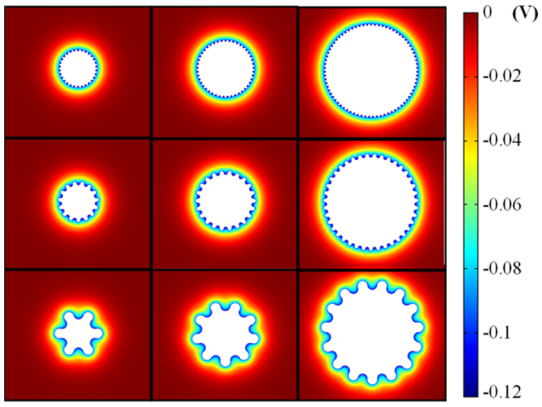

Figure 4. Potential distributions of different particle diameters and roughness diameters at pH = 7 and C_{KCl} = 1 mM. Particle diameter increases from left to right when the roughness diameter is constant, and the roughness diameter increases from bottom to top when the particle diameter is constant (D_P = 40, 60, and 100 nm; D_R = 2, 4, and 10 nm).

As a next step, distributions of local surface charge densities were measured based on the ionic potential formed on the surface. Figure 5 gives the distribution of surface charge on the nanoparticle surfaces along the normalized radial position ($r/\pi D_R$). Also, average of these local surface charge densities along the roughness was calculated for each case. For comparison, the surface charge density of a flat nanoparticle at the corresponding particle diameter without any roughness and the surface charge density of a flat planar surface were also calculated and added on the graph for each case. The surface charge of a flat plate can be calculated from the classical PB theory easily.[79,80] Although the flat plate surface charge is the same for all cases ($\sigma_{flat\text{-}plate}$ = −0.013718 C/m^2 at 1 mM and pH = 7), the flat nanoparticle surface charge shows variation by the particle diameter ($\sigma_{flat\text{-}particle\text{-}100nm}$ = −0.014079 C/m^2, $\sigma_{flat\text{-}particle\text{-}60nm}$ = −0.014312 C/m^2, and $\sigma_{flat\text{-}particle\text{-}40nm}$ = −0.014598 C/m^2). Simply, with the decrease of the particle

https://dx.doi.org/10.1021/acs.jpcc.0c00120
J. Phys. Chem. C 2020, 124, 7274−7286

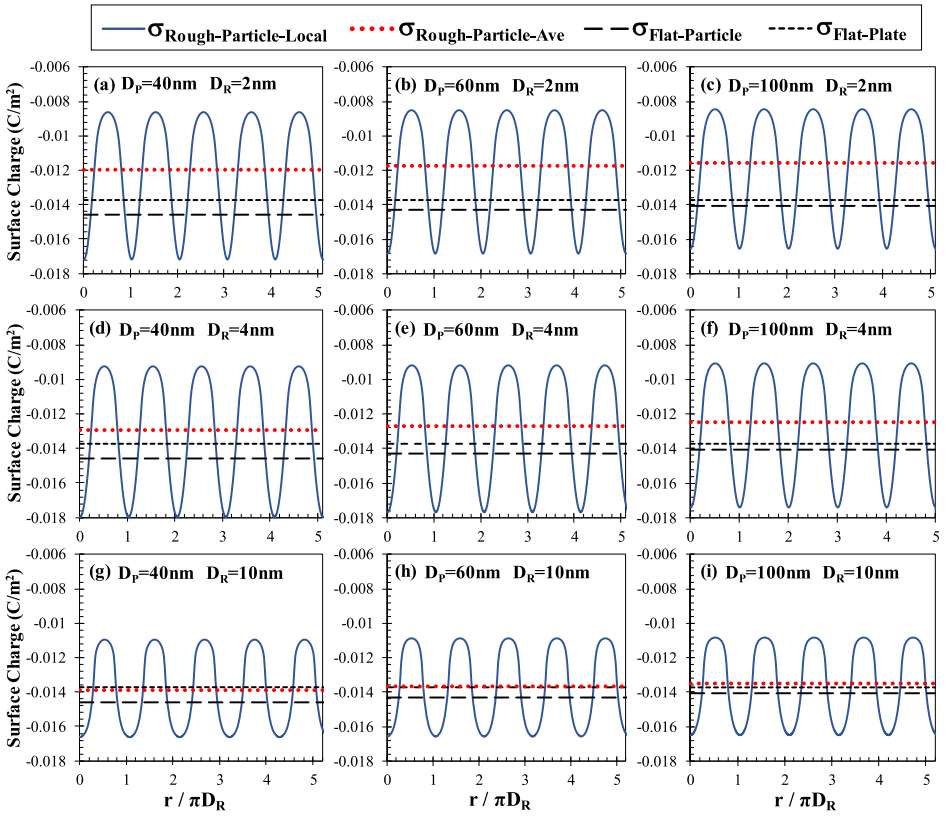

Figure 5. Surface charge density distribution through the arc length of the surface pattern around nanoparticles with different particle diameters (D_P = 40, 60, and 100 nm) and roughness diameters (D_R = 2, 4, and 10 nm).

diameter, the absolute value of surface charge of the flat nanoparticle increases and becomes higher than the absolute value of the flat plate surface charge. This size-dependent surface charge of nanoparticles develops because of the so-called curvature effects becoming dominant for particles, especially, smaller than 50 nm in diameter.[19]

The surface charge around the rough nanoparticle varies along the patterned surface, but the variation repeats itself over every surface structure. Even though the number of surface structures is different for each case, we only presented the surface charge density over five surface structures because the remaining will be identical. EDL overlap starts at the deep of the valley and decreases toward the top region of the roughness geometry. The absolute value of surface charge is lower in the valleys and higher on the hills than the flat plate value because of EDL overlap and the curvature effect, respectively. The absolute value of charge on the hills are even higher than the value of the flat nanoparticle because the curvature effects are higher as the diameter of roughness is smaller. The absolute value of the average of local surface charge distribution yields lower values than the corresponding flat plate and flat nanoparticle surface charge predictions. This difference decreases as the roughness diameter increases. Basically, both EDL overlap and curvature effects decrease with an increase in the size of roughness structures. This also shows itself as decreasing fluctuations in the local variation of the nanoparticle surface charge.

Next, we study the surface charge developing at the top point of the hill and at the bottom point of the valley. These are the highest and lowest surface charges observed through local variation from Figure 6. Here, a wide range of particle (D_P = 10, 20, 40, 60, 100, and 200 nm) and roughness (D_R = 1,

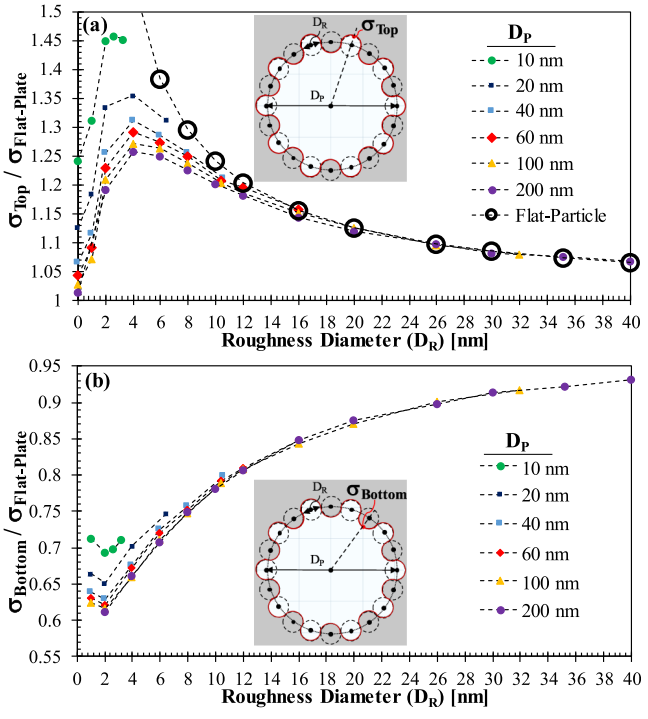

Figure 6. Normalized surface charge density distributions at the (a) top and (b) bottom points of the roughness structure as a function of the roughness diameter for different particle diameters (C_{KCl} = 1 mM, pH = 7).

2, 3, 4, 6, 10, 12, 16, 20, 26, 30, 36, and 40 nm) diameters were studied. For 200 nm particle size, all of the roughness

https://dx.doi.org/10.1021/acs.jpcc.0c00120
J. Phys. Chem. C 2020, 124, 7274−7286

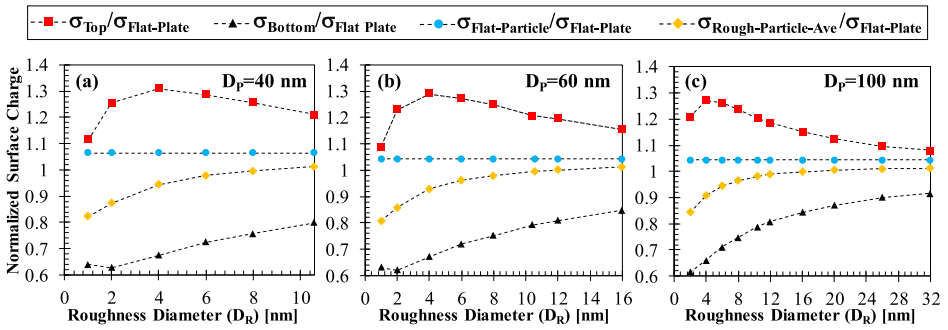

Figure 7. Normalized surface charge densities measured locally at the top and bottom regions accompanied by the average surface charge measured around the rough nanoparticle for different particle diameters: (a) D_P = 40 nm, (b) D_P = 60 nm, and (c) D_P = 100 nm.

diameters listed above were studied. However, by decreasing the particle size, possible roughness diameters lessened; simply, we tried to keep D_R less than ∼1/4 of D_P. Figure 6 presents the surface charge density values measured at the top (Figure 6a) and bottom (Figure 6b) of roughness geometry normalized with the surface charge of classical flat plate theory prediction.

In Figure 6a, the variation of the surface charge measured at the tip of the surface structure as a function of the size of the structure (D_R) is presented for different size nanoparticles (D_P). For comparison purposes, the normalized surface charge values of a flat nanoparticle at the corresponding roughness diameter are also given. Overall, surface charges are higher than flat plate calculations because of curvature effects. Pure curvature effects can be directly observed from the constant increase of surface charge of the flat nanoparticle (no surface roughness) with decreasing particle size (equal to the roughness diameter in this graph). It can also be easily seen that the curvature effects disappear with an increase in size as the surface charge on a flat nanoparticle becomes equal to the surface charge calculated for a flat plate (no curvature). Through this extent, the surface charge on the tip of a circular surface pattern develops curvature effects identical to those of a flat nanoparticle, with the particle diameter equal to the corresponding roughness diameter. Such behavior develops for roughness diameters equal and greater than 12 nm; by the decrease of the roughness diameter, the tip surface charge increases up to 1.2 times of the flat plate value at 12 nm. This increase is independent of the diameter of the rough nanoparticle; for example, tips of D_R = 12 nm surface pattern of 40, 60, 100, and 200 nm rough nanoparticle develops similar surface charges with each other and with12 nm flat nanoparticle. For roughness diameters smaller than 10 nm, EDL overlap effects growing strong from the valleys start affecting the tips of the hills that the surface charges of the tip first slow their increase, later reach a plateau, and then start decreasing on decreasing the roughness diameter. In this range of roughness diameter, the variation of the tip surface charge depends strongly on the diameter of the rough particle. We also added the surface charge of each nanoparticle measured in the case of no surface structure on this figure as zero surface roughness value. Interestingly, the variation of measured tip values and flat nanoparticle values showed a complete trend. This offers clues for continuum representation about how the surface charge approaches flat surface behavior through both limits of surface roughness ($0 \rightarrow \infty$). Basically, the surface charge reaches the flat surface nanoparticle value as the roughness disappears ($D_R \rightarrow 0$), whereas the local surface charge converges to flat plate behavior as the roughness grows and the curvature disappears ($D_R \rightarrow \infty$).

Figure 6b presents the variation of surface charge measured at the bottom point of the valleys of the surface pattern for the different size rough nanoparticles with different roughness diameters. Opposite to the top surface charge, the surface charges at the bottom are lower than the flat plate prediction as a result of the EDL overlap. The bottom point surface charge decreases with a decrease in the roughness diameter as the EDL overlap increases. Conversely, with an increase in the roughness diameter, the surface becomes flatter that the bottom surface charge converges to the flat surface charge value calculated by theory. Similar to the behavior of the top surface charge, variations of the bottom surface charge of different size rough nanoparticles are very similar, except for the roughness diameters lower than 12 nm. As the growing EDL overlap from the bottom affects the top, this interaction also affects the behavior developing at the bottom point. When observing these two graphs (Figure 5a,b), we can understand how these two opposite effects developing at the two ends of the surface structure influence each other by decreasing the roughness size.

After resolving the behavior of the highest and lowest electric charges developing on a rough surface, we studied the average of local surface charge varying in between. Simply, we calculated the average of surface charge distributions shown in Figure 5. Figure 7 presents the variation of top and bottom surface charges together with the average surface charge as a function of the surface roughness diameter for rough particles of 40, 60, and 100 nm in diameter. For comparison, the surface charge of a flat nanoparticle at the corresponding particle diameters of 40, 60, and 100 nm is also given. All charge values are normalized by the surface charge calculated from the flat plate theory. Overall, the average of local surface charges developing around the rough nanoparticle is lower than that for the flat particle with the same diameter. This difference increases on decreasing the roughness diameter. The difference between the top and bottom surface charges and hence the difference between the average charge of the rough particle and the charge of the flat particle decreases when the roughness diameter increases.

Next, the average surface charges of different diameter rough nanoparticles were given together to compare their behavior as a function of the surface roughness diameter in Figure 8. To illustrate the geometrical variation by the roughness diameter, rough nanoparticle shapes of 60 nm particle diameter with the electric potential contours are given in the figure. Overall, there is a 20% decrease from the flat plate theory on decreasing the

https://dx.doi.org/10.1021/acs.jpcc.0c00120
J. Phys. Chem. C 2020, 124, 7274−7286

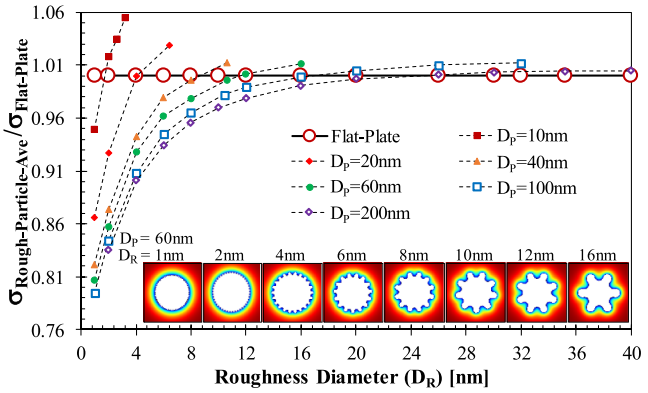

Figure 8. Variation of the average surface charge density measured along the arc length of the surface pattern by varying the roughness and particle diameter (C_{KCl} = 1 mM, pH = 7). The roughness diameter variation is also given for the 60 nm diameter particle in the figure.

roughness diameter. On the opposite end, the average surface charge approaches that of the flat surface theory with an increase in both the particle diameter and roughness diameter. This behavior is a function of the particle diameter. For example, the surface charge of the 200 nm rough particle with roughness diameters higher than 26 nm reaches the flat plate value. On the other hand, at lower particle diameters, the surface charge converges to higher values than the flat plate surface charge because of the curvature effect of the small particle size.

Up to this point, we kept the pH value of the ionic solution at 7. Next, we studied the effect of pH variation on surface charging. Surface charge as a function of pH is a well-known behavior described by the titration experiments.[70] The pH-dependent surface charge of flat nanoparticles is described in our earlier study[19] and by the subsequent work.[61] The average surface charge of 40, 60, and 100 nm rough nanoparticles is given as a function of pH for different roughness diameters in Figure 9. Surface charges are normalized by the theoretical flat plate charge value. Flat particle surface charge is higher than that of the flat plate, and this difference is the highest at medium pH levels between 5 and 6. With an increase or decrease in pH from this midlevel, the surface charge of the flat particle decreases. A rough nanoparticle presents opposite behavior; surface charge values are lower than the flat plate value, and the lowest value develops at medium pH levels. This mid-pH value eventually moves from left to right by the decrease of the roughness diameter. Interestingly, with the increase in the roughness diameter, the surface charge of rough particles first reaches the flat plate value and later approaches the flat particle behavior. The pH-dependent variation of the surface charge shows a very similar trend for different nanoparticle diameters, but the surface charge values for a given surface roughness diameter and pH are different on different size nanoparticles. On the other hand, very similar surface charge values and pH-dependent variations develop at different roughness diameters of different size particles. For instance, D_R = 10 nm of D_P = 40 nm, D_R = 16 nm of D_P = 60 nm, and D_R = 24 nm of D_P = 100 nm develops very similar surface charge values and pH-dependent variations. This gives us the first indication of the existence of the universal surface charging behavior of rough nanoparticles.

For the purpose of proper characterization, we consolidated the results together in Figure 10. Surface charges of rough nanoparticles of 40, 60, 100, and 200 nm in diameter are plotted for different pH levels as a function of the surface roughness. The surface charge densities are normalized by the flat plate value at the corresponding ionic concentration and pH. In this presentation of data, there is a complex variation which does not depict universal behavior. Similar to our earlier experience,[66] some cases show similar trends and form groups among themselves, but a clear relationship is hard to obtain. This shows that characterization based on roughness diameter only is not adequate.

A three-dimensional presentation of the variation of the normalized surface charge of a rough nanoparticle as a function of pH and roughness diameter is given in Figure 11. This representation helps us to observe that the surface charge variation shows similar behavior between different size nanoparticles with a shift.

It appears that, for proper characterization, we must focus on each of the charging mechanisms on the rough surface, which are EDL overlap in the valleys, curvature effects on the hills, and curvature effect over the particle itself. First of all, characterization of curvature effects of nanoparticles was done in our earlier study in detail.[19] We showed that the decrease of nanoparticle size reduces the volume-to-surface ratio, which yields significant deviation of nanoparticle ion distribution from the planar surface behavior. In such a case, we presented that the curvature effect of a nanoparticle can be estimated by the ratio of the EDL thickness (λ) to the particle diameter (λ/

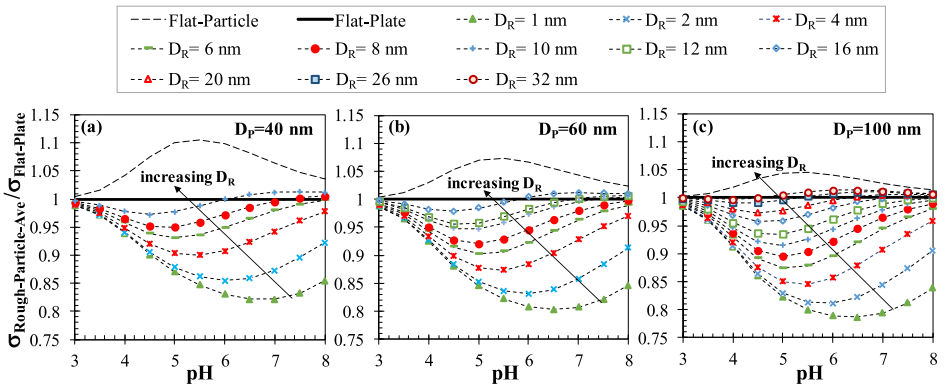

Figure 9. Comparison of the surface charge of flat plate, flat particle, and rough particles with different roughness diameters according to the pH. Each graph has a constant particle diameter of (a) D_P = 40 nm, (b) D_P = 60 nm, and (c) D_P = 100 nm at C_{KCl} = 1 mM and pH = 7.

https://dx.doi.org/10.1021/acs.jpcc.0c00120
J. Phys. Chem. C 2020, 124, 7274−7286

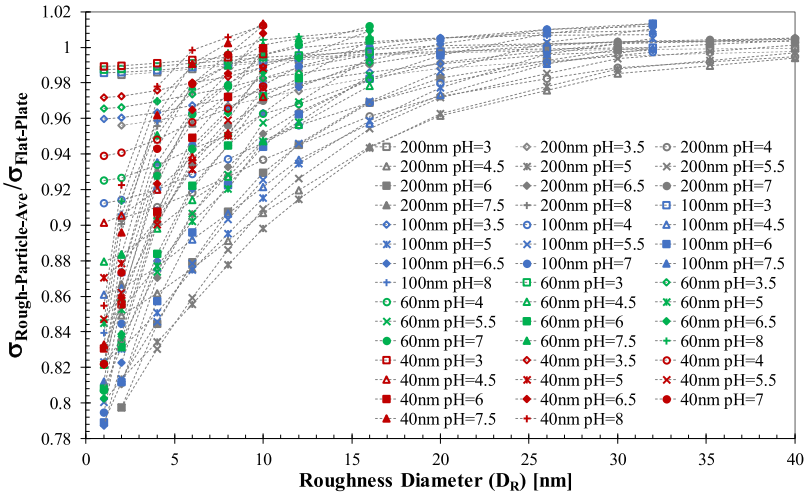

Figure 10. Variation of the average surface charge of rough nanoparticles of different particle diameters (D_P = 40, 60, 100, and 200 nm) at different pH levels as a function of the roughness diameter.

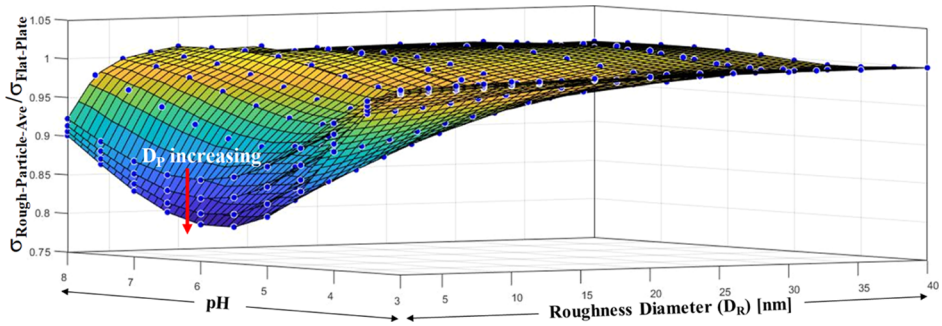

Figure 11. Variation of the average surface charge of rough nanoparticles of different particle diameters (D_P = 40, 60, 100, and 200 nm) as a function of pH and roughness diameter.

D_P); when D_P is comparable to λ ($\lambda/D_P > 0.2$[19]), curvature effects develop, and decrease of D_P continuously increases it. Here, the surface charge of the nanoparticle increases with the increase of λ/D_P. Second, in a separate study, we characterized the surface charge formation of a planar surface with the roughness of repeating concave and convex circles, similar to the current investigation.[66] We presented that the degree of overlap in the valleys can be estimated by the ratio of the EDL thickness (λ) to the valley size defined as the roughness dimeter, D_R. Similarly, the degree of curvature on the hills can also be approximated by λ/D_R. Here, again when λ/D_R becomes higher than 0.2, surface charging deviates from flat surface calculations; but differently, decrease of D_R first increases the deviations, but later, the electric potential on the rough surface flattens and approaches back to the flat surface calculations.[66] Through the roughness, the curvature effect of hills creates higher surface charges, whereas EDL overlap of valleys develops lower surface charges than the flat plate charge value. Ultimately, these two cancel each other, but by decreasing λ/D_R, EDL overlap grows over the hills and lessens the curvature effects; as a result, roughness yields an average surface charge lower than the flat plate charge value.

In the current case of a nanoparticle with surface roughness, we have the combination of these two occurrences in a coupled manner. Roughness effects develop as a function of λ/D_R, but their variation differs by the nanoparticle diameter D_P. Roughness effects create surface charges lower than that of the flat plate, but this divergence lessens by the decrease of D_P.

For example, Figure 8 shows that at a certain D_R, roughness effects decrease as the particle diameter decreases. Using these observations and our earlier experience, we attempted to characterize the rough nanoparticle surface charge as a function of D_R/λ and D_R/D_P. We observed that the surface charge variation showed universal behavior at a constant pH. We present the variation of the average rough nanoparticle surface charge as a function of $(D_R/\lambda) \times (D_R/D_P)$ at each pH level in Figure 12. At a given pH, the surface charge of different diameter particles diverges from the flat plate value with a similar behavior by the decrease of square of roughness diameter normalized by the EDL thickness and the corresponding particle diameter. Divergence from the flat plate calculations is the highest at moderate pH values around pH = 6 and pH = 7. For low pH values between pH = 3 and pH = 5.5, variation of surface charge slows down.

Figure 12 shows that the nondimensional group of $(D_R/\lambda) \times (D_R/D_P)$ appears as a proper set of parameters to describe the surface charging of a rough nanoparticle. The surface charge exponentially decreases by the decrease of $D_R^2/(\lambda \times D_P)$ parameter that the rough nanoparticle surface charge can be simply defined with respect to analytical flat plate calculations as

$$\frac{\sigma_{\text{rough-particle-ave}}}{\sigma_{\text{flat-plate}}} = 1 - A \times \exp\left(-B \times \left(\frac{D_R^{\,2}}{D_P \times \lambda}\right)\right) \quad (11)$$

https://dx.doi.org/10.1021/acs.jpcc.0c00120
J. Phys. Chem. C 2020, 124, 7274−7286

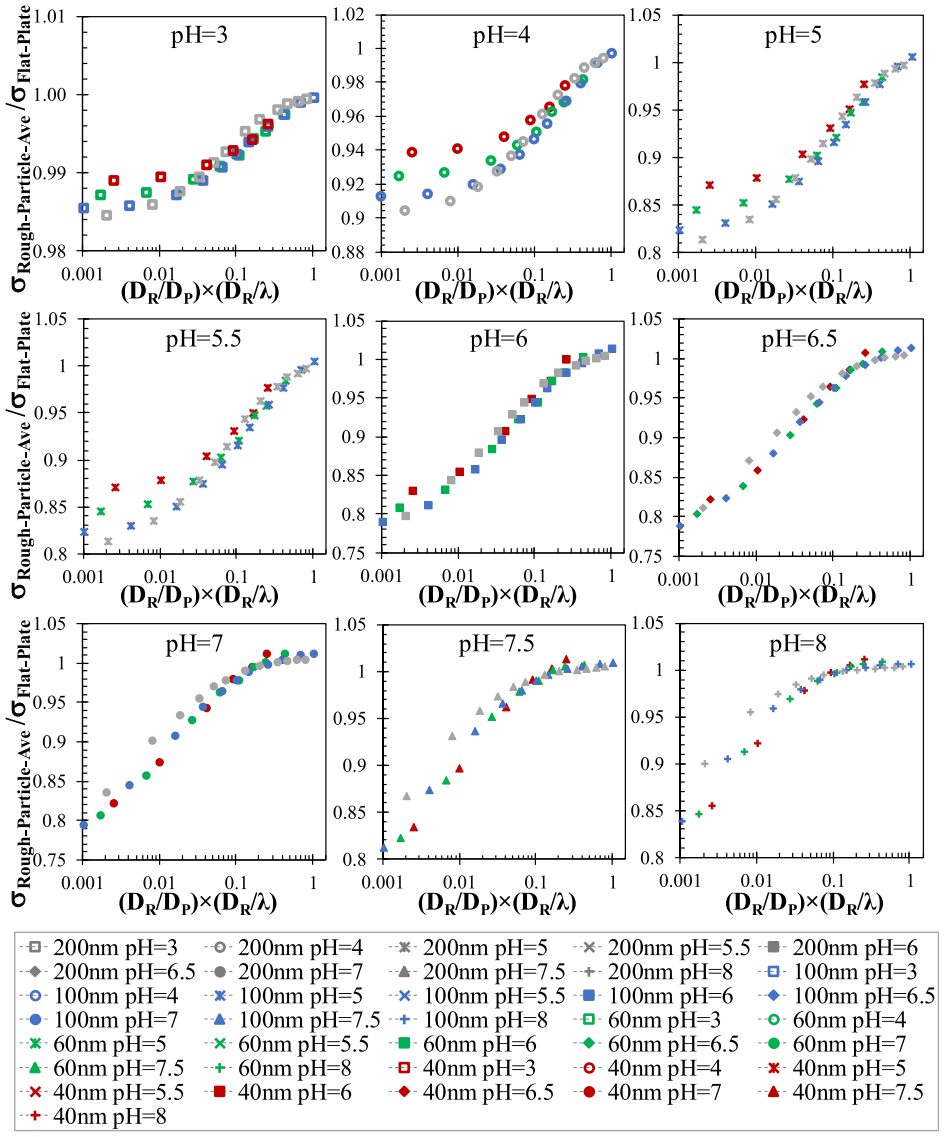

Figure 12. Variation of the average surface charge of rough nanoparticles of different particle and roughness diameters at different pH levels.

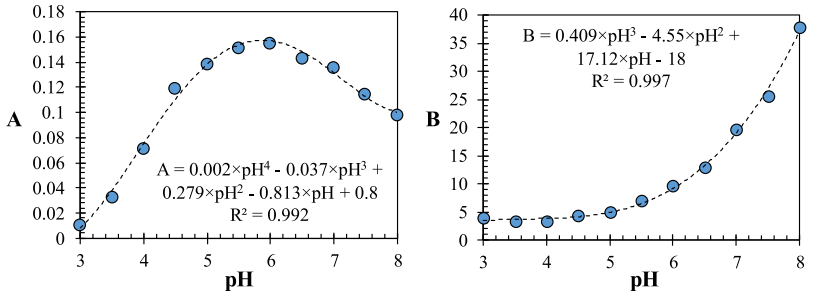

Figure 13. Variation of the *A* and *B* constants for eq 6 at every pH level.

where *A* and *B* are constants varying by pH. We applied eq 11 onto each group of results of different diameter particles at a constant pH value presented in Figure 12 and determined *A* and *B* constants. Figure 13 presents the calculated *A* and *B* constants for each pH level.

We observed that fourth- and third-order polynomial functions of pH describes well the variations of A and B parameters, with R^2 parameters close to unity.

$$A = 0.002 \times pH^4 - 0.037 \times pH^3 + 0.279 \times pH^2 - 0.813 \times pH + 0.8 \quad (12)$$

$$B = 0.409 \times pH^3 - 4.55 \times pH^2 + 17.12 \times pH - 18 \quad (13)$$

Next, we tested the success of the extended model. We compared the surface charge predictions of eqs 11−13 with our numerical results. Figure 14 presents the difference as a

https://dx.doi.org/10.1021/acs.jpcc.0c00120
J. Phys. Chem. C 2020, 124, 7274−7286

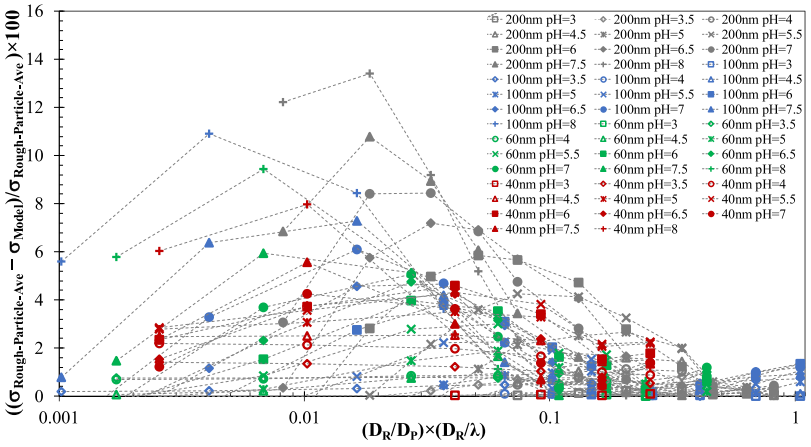

Figure 14. Variation of relative error as a percentile difference between the numerical results and the devised extended model given through eqs 11−13.

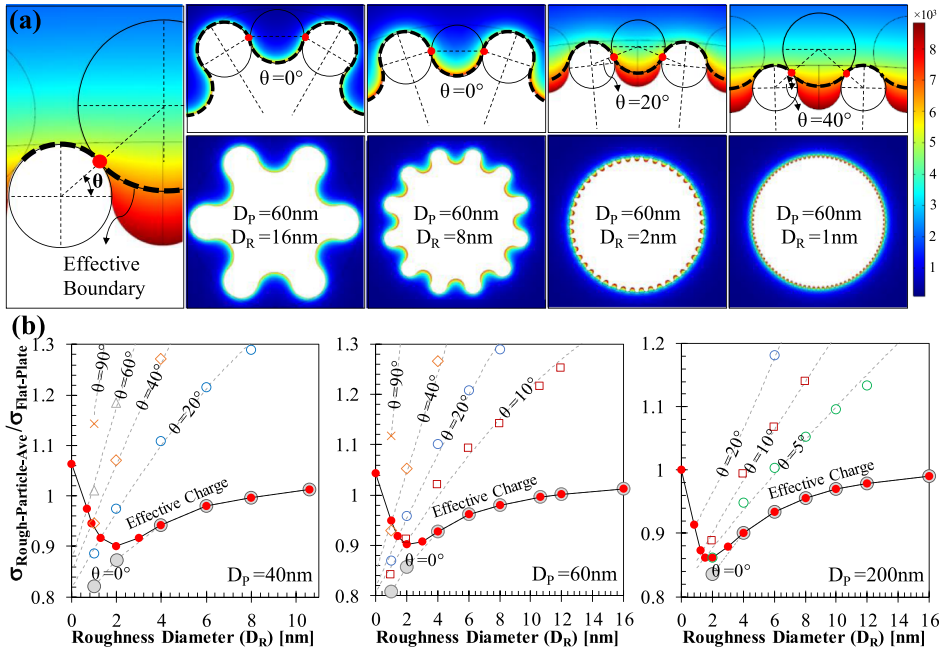

Figure 15. (a) Description of the angle θ to define the effective boundary for electrokinetic interactions of a rough nanoparticle and its variation by the roughness diameter presented for a 60 nm particle [contours are for the ionic concentration of hydrogen (mol/m^3)]. (b) Possible divergence of the surface charge from the calculated surface charge measured through the arc length path of surface structures (θ = 0°) with the decrease of the roughness diameter below 3 nm for 40, 60, and 200 nm particles.

percentile. Error values mostly remain lower than 5%, and the highest error is around 13% for only one case.

As a final discussion, we contemplated about a possible boundary description around the rough nanoparticle, which would be effective in the electrostatic interactions with other entities. The so called "effective boundary" condition on a rough surface has been investigated for fluid dynamics by many researchers,[81−83] but the electric boundary condition on a rough surface is mostly overlooked by the literature. As the roughness diameter decreases, the surface becomes flattened. We observed this through the electric potential distributions given earlier in Figure 4, where the potential developed around the nanoparticle with small surface roughness presents a smooth distribution. This is due to the high EDL overlap growing out of surface roughness. For such a case, any electrostatic or electrokinetic interaction between an object and a rough/patterned nanoparticle would be governed by the electric properties at the effective boundary region rather than the electric charge at the bottom of the surface patterns. Based on this perspective, we hypothesized an effective electric boundary condition in the form of circular arcs between hills parallel to the arcs of surface patterns in the valleys. Simply, this effective charge boundary is a combination of concave and convex circular arcs on the hills and valleys similar to the surface structure of the nanoparticle; but differently, convex circular arcs extend and widen out of the valleys with the decrease of the roughness diameter. To describe this, we used an angle θ defining the point where the concave circular arc of the hill meets with the convex arc of the valley. In the normal definition, the surface pattern is a form of half circles and θ = 0°. By the decrease of D_R, the angle θ increases and the effective boundary flattens. At θ = 90°, the effective boundary becomes a complete circle around the particle passing through the tips of the hills. We illustrated the effective boundary for

https://dx.doi.org/10.1021/acs.jpcc.0c00120
J. Phys. Chem. C 2020, 124, 7274−7286

electrokinetics and its variation by the roughness diameter for the 60 nm particle in Figure 15a using the ionic concentration contours of hydrogen.

Next, we practiced this perspective to determine an effective charge on rough nanoparticles. We measured the surface charges through the boundaries of different θ angles around 40, 60, and 200 nm particles at various roughness diameters (Figure 15b). We applied a linear fit onto the data set of each constant θ case to define their variation. While the effective charge is equal to the charge measured through the arc length path of surface structures ($\theta = 0°$) with the decrease of the roughness diameter, the effective charge will differentiate and approach toward charges measured through the higher θ value boundaries. Ultimately, a decrease in the electric charge on decreasing the roughness diameter stops, and then the electric charge starts to increase toward the surface charge value measured on a flat particle ($D_R = 0$) of the corresponding particle diameter. This is a very interesting and expected behavior. We should also mention that the flat surface theory and so this new extended model is applicable on cases where continuum assumption remained valid. The primary surface charging develops on the binding sites, which is usually described by the site density per area. Whereas the different experimental procedures reported different results, the site density for silica is mostly measured between 5 and 11 sites/nm^2.[84] There are positively and negatively charged surface groups distributed on these binding sites, and the continuum description of corresponding surface charge is approximated by the average of these surface groups. Such an average definition will not be appropriate for small bodies because there will not be enough binding sites for proper statistical averaging. Hence, the current continuum calculations and the proposed empirical model are not appropriate to estimate surface charging for roughness sizes smaller than ~2 nm. This means D_R values less than certain scales ($D_R < 2$ nm) cannot be predicted by PNP or by our extended model given in eqs 11−13.

CONCLUSIONS

We characterized the surface charge density of the rough SNPs. In contrast to many studies considering the surface charge independent of the particle size and the surface topography, this study calculated the effects of nanoparticle surface structures on surface charging. Using the numerical solution of ionic equilibrium based on PNP equation with CR boundaries, we found that the surface charge density is not just a material property, but it depends on the size of the nanoparticle and the size of its surface roughness, in addition to the solution conditions. In this regard, we calculated the local surface charge density based on the local ionic concentrations for various particle and roughness diameters. Through such a systematic approach, we evaluated both local and average surface charge density and observed the variation as a function of EDL overlaps and curvature effects through the surface of a rough nanoparticle. In general, as the roughness diameter decreases, the EDL overlap developing in the valleys of the pattern decreases the local surface charge, whereas curvature effects developing on the hills increase the local charges. Hence, the homogeneous surface charge assumption is invalid even at this continuum level; charge values can be up to 40% lower in the valleys and 30% higher on the hills compared to the theoretical predictions for a flat plate. We characterized simultaneous behavior of these two opposite mechanisms by calculating an average charge value around the rough nanoparticle. For the current representative pattern made of repeating circular hills and valleys of identical size, decreases in the surface charge in the valleys and increases on the hills almost cancel each other up to a certain value of roughness diameter that the average surface charge remains close to the surface charge of a flat surface. However, with the decrease in the roughness diameter, the average surface charge decreases, depending on the particle diameter and pH. We characterized the overall behavior in terms of particle diameter, roughness diameter, and pH by defining a nondimensional group as $(D_R/\lambda) \times (D_R/D_P)$. We observed unified behavior through the results of different diameter particles at different roughness values as a function of $(D_R/\lambda) \times (D_R/D_P)$ that we devised a phenomenological model describing the deviation of average charge density of a rough nanoparticle from the flat surface theory. The proposed model extends the existing theory as a function of particle and roughness diameters at various pH levels successfully. This model has a certain roughness size limit ($D_R > 2$ nm) below which the ionic distribution around the rough nanoparticle flattens, and eventually, the nanoparticle surface charge approaches back to predictions of the flat surface theory. We demonstrated this in continuum level by defining an effective boundary for electric condition around a rough nanoparticle. Current results recommend that surface heterogeneity creates dominant effects on surface charge formation of nanoparticles for the first time in the literature. Variation of the surface area per mass at a constant nanoparticle size eventually shows the variation of surface structural conditions (such as the roughness diameter) in the current literature; however, any resulted variation in the surface charge or zeta potential of the nanoparticle by surface roughness is overlooked. Although such behavior creates complications for many applications, it can also be advantageous for future technologies that nanoengineered surface conditions can be designed with the desired surface charging for the desired task.

AUTHOR INFORMATION

Corresponding Author

Murat Barisik − *Department of Mechanical Engineering, Izmir Institute of Technology, Izmir 35430, Turkey;* orcid.org/0000-0002-2413-1991; Email: muratbarisik@iyte.edu.tr

Authors

B. Oyku Alan − *Department of Mechanical Engineering, Izmir Institute of Technology, Izmir 35430, Turkey*

H. Gokberk Ozcelik − *Department of Mechanical Engineering, Izmir Institute of Technology, Izmir 35430, Turkey*

Complete contact information is available at: https://pubs.acs.org/10.1021/acs.jpcc.0c00120

Notes

The authors declare no competing financial interest.

ACKNOWLEDGMENTS

This work was supported by the Scientific and Technological Research Council of Turkey (TUBITAK) under the grant number 118M710. The authors would also like to thank the Center for Scientific Computation at Southern Methodist University.

REFERENCES

(1) Liong, M.; Lu, J.; Kovochich, M.; Xia, T.; Ruehm, S. G.; Nel, A. E.; Tamanoi, F.; Zink, J. I. Multifunctional Inorganic Nanoparticles for Imaging, Targeting, and Drug Delivery. *ACS Nano* **2008**, *2*, 889.

(2) Lee, J. E.; Lee, N.; Kim, T.; Kim, J.; Hyeon, T. Multifunctional Mesoporous Silica Nanocomposite Nanoparticles for Theranostic Applications. *Acc. Chem. Res.* **2011**, *44*, 893.

(3) Slowing, I. I.; Trewyn, B. G.; Giri, S.; Lin, V. S. Y. Mesoporous Silica Nanoparticles for Drug Delivery and Biosensing Applications. *Adv. Funct. Mater.* **2007**, *17*, 1225.

(4) Popat, A.; Hartono, S. B.; Stahr, F.; Liu, J.; Qiao, S. Z.; Lu, G. Q. Mesoporous Silica Nanoparticles for Bioadsorption, Enzyme Immobilisation, and Delivery Carriers. *Nanoscale* **2011**, *3*, 2801.

(5) Ariga, K.; Ji, Q.; Mori, T.; Naito, M.; Yamauchi, Y.; Abe, H.; Hill, J. P. Enzyme Nanoarchitectonics: Organization and Device Application. *Chem. Soc. Rev.* **2013**, *42*, 6322.

(6) Li, Z.; Barnes, J. C.; Bosoy, A.; Stoddart, J. F.; Zink, J. I. Mesoporous Silica Nanoparticles in Biomedical Applications. *Chem. Soc. Rev.* **2012**, *41*, 2590.

(7) Vivero-Escoto, J. L.; Slowing, I. I.; Lin, V. S. Y.; Trewyn, B. G. Mesoporous Silica Nanoparticles for Intracellular Controlled Drug Delivery. *Small* **2010**, *6*, 1952.

(8) Yang, P.; Gai, S.; Lin, J. Functionalized Mesoporous Silica Materials for Controlled Drug Delivery. *Chem. Soc. Rev.* **2012**, *41*, 3679.

(9) Zhang, M.; Yeh, L.-H.; Qian, S.; Hsu, J.-P.; Joo, S. W. DNA Electrokinetic Translocation through a Nanopore: Local Permittivity Environment Effect. *J. Phys. Chem. C* **2012**, *116*, 4793−4801.

(10) Ai, Y.; Liu, J.; Zhang, B.; Qian, S. Field Effect Regulation of DNA Translocation through a Nanopore. *Anal. Chem.* **2010**, *82*, 8217.

(11) Li, X.; Xie, Q. R.; Zhang, J.; Xia, W.; Gu, H. The Packaging of SiRNA within the Mesoporous Structure of Silica Nanoparticles. *Biomaterials* **2011**, *32*, 9546.

(12) Xiao, D.; Jia, H. Z.; Ma, N.; Zhuo, R. X.; Zhang, X. Z. A Redox-Responsive Mesoporous Silica Nanoparticle Capped with Amphiphilic Peptides by Self-Assembly for Cancer Targeting Drug Delivery. *Nanoscale* **2015**, *7*, 10071.

(13) Kwon, S.; Singh, R. K.; Perez, R. A.; Neel, E. A. A.; Kim, H. W.; Chrzanowski, W. Silica-Based Mesoporous Nanoparticles for Controlled Drug Delivery. *J. Tissue Eng.* **2013**, *4*, 204173141350335.

(14) Santos, H. A.; Mäkilä, E.; Airaksinen, A. J.; Bimbo, L. M.; Hirvonen, J. Porous Silicon Nanoparticles for Nanomedicine: Preparation and Biomedical Applications. *Nanomedicine* **2014**, *9*, 535.

(15) Kinnari, P.; Mäkilä, E.; Heikkilä, T.; Salonen, J.; Hirvonen, J.; Santos, H. A. Comparison of Mesoporous Silicon and Non-Ordered Mesoporous Silica Materials as Drug Carriers for Itraconazole. *Int. J. Pharm.* **2011**, *414*, 148.

(16) Schwartz, M. P.; Yu, C.; Alvarez, S. D.; Migliori, B.; Godin, D.; Chao, L.; Sailor, M. J. Using an Oxidized Porous Silicon Interferometer for Determination of Relative Protein Binding Affinity through Non-Covalent Capture Probe Immobilization. *Phys. Status Solidi A* **2007**, *204*, 1444.

(17) Perrault, S. D.; Walkey, C.; Jennings, T.; Fischer, H. C.; Chan, W. C. W. Mediating Tumor Targeting Efficiency of Nanoparticles through Design. *Nano Lett* **2009**, *9*, 1909.

(18) Cho, K.; Wang, X.; Nie, S.; Chen, Z.; Shin, D. M. Therapeutic Nanoparticles for Drug Delivery in Cancer. *Clin. Cancer Res.* **2008**, *14*, 1310.

(19) Barisik, M.; Atalay, S.; Beskok, A.; Qian, S. Size Dependent Surface Charge Properties of Silica Nanoparticles. *J. Phys. Chem. C* **2014**, *118*, 1836−1842.

(20) Argyo, C.; Weiss, V.; Bräuchle, C.; Bein, T. Multifunctional Mesoporous Silica Nanoparticles as a Universal Platform for Drug Delivery. *Chem. Mater.* **2014**, *26*, 435.

(21) Slowing, I.; Trewyn, B. G.; Lin, V. S. Y. Effect of Surface Functionalization of MCM-41-Type Mesoporous Silica Nanoparticles on the Endocytosis by Human Cancer Cells. *J. Am. Chem. Soc.* **2006**, *128*, 14792.

(22) Forest, V.; Cottier, M.; Pourchez, J. Electrostatic Interactions Favor the Binding of Positive Nanoparticles on Cells: A Reductive Theory. *Nano Today* **2015**, *10*, 677.

(23) Shang, L.; Nienhaus, K.; Nienhaus, G. U. Engineered Nanoparticles Interacting with Cells: Size Matters. *J. Nanobiotechnol.* **2014**, *12*, 5.

(24) Koike, N.; Chaikittisilp, W.; Shimojima, A.; Okubo, T. Surfactant-Free Synthesis of Hollow Mesoporous Organosilica Nanoparticles with Controllable Particle Sizes and Diversified Organic Moieties. *RSC Adv* **2016**, *6*, 90435.

(25) Kang, J. S.; Lim, J.; Rho, W. Y.; Kim, J.; Moon, D. S.; Jeong, J.; Jung, D.; Choi, J. W.; Lee, J. K.; Sung, Y. E. Wrinkled Silica/Titania Nanoparticles with Tunable Interwrinkle Distances for Efficient Utilization of Photons in Dye-Sensitized Solar Cells. *Sci. Rep.* **2016**, *6*, 30829.

(26) Shi, Y.-R.; Ye, M. P.; Du, L. C.; Weng, Y. X. Experimental Determination of Particle Size-Dependent Surface Charge Density for Silica Nanospheres. *J. Phys. Chem. C* **2018**, *122*, 23764.

(27) Kobayashi, M.; Juillerat, F.; Galletto, P.; Bowen, P.; Borkovec, M. Aggregation and Charging of Colloidal Silica Particles: Effect of Particle Size. *Langmuir* **2005**, *21*, 5761.

(28) Borghi, F.; Vyas, V.; Podestà, A.; Milani, P. Nanoscale Roughness and Morphology Affect the IsoElectric Point of Titania Surfaces. *PLoS One* **2013**, *8*, No. e68655.

(29) Duval, J. F. L.; Leermakers, F. A. M.; Van Leeuwen, H. P. Electrostatic Interactions between Double Layers: Influence of Surface Roughness, Regulation, and Chemical Heterogeneities. *Langmuir* **2004**, *20*, 5052.

(30) Yang, X.; Zhang, G. The Effect of an Electrical Double Layer on the Voltammetric Performance of Nanoscale Interdigitated Electrodes: A Simulation Study. *Nanotechnology* **2008**, *19*, 465504.

(31) Božič, A. L. From Discrete to Continuous Description of Spherical Surface Charge Distributions. *Soft Matter* **2018**, *14*, 1149.

(32) Blanco, M. A.; Shen, V. K. Effect of the Surface Charge Distribution on the Fluid Phase Behavior of Charged Colloids and Proteins. *J. Chem. Phys.* **2016**, *145*, 155102.

(33) Abrikosov, A. I.; Stenqvist, B.; Lund, M. Steering Patchy Particles Using Multivalent Electrolytes. *Soft Matter* **2017**, *26*, 4591.

(34) Bianchi, E.; van Oostrum, P. D. J.; Likos, C. N.; Kahl, G. Inverse Patchy Colloids: Synthesis, Modeling and Self-Organization. *Curr. Opin. Colloid Interface Sci.* **2017**, *30*, 8.

(35) Yang, Y.; Webb, K.; Liu, Y.; Liu, K.; Nie, Z. Synthesis, Self-Assembly, and Applications of Amphiphilic Janus and Triblock Janus Nanoparticle Analogs. In *Soft, Hard, and Hybrid Janus Structures: Synthesis, Self-assembly, and Applications*; World Scientific, 2017.

(36) Palleau, E.; Ressier, L.; Borowik, Ł.; Mélin, T. Numerical Simulations for a Quantitative Analysis of AFM Electrostatic Nanopatterning on PMMA by Kelvin Force Microscopy. *Nanotechnology* **2010**, *21*, 225706.

(37) Hoogenboom, J. P.; Vossen, D. L. J.; Faivre-Moskalenko, C.; Dogterom, M.; Van Blaaderen, A. Patterning Surfaces with Colloidal Particles Using Optical Tweezers. *Appl. Phys. Lett.* **2002**, *80*, 4828.

(38) Parthasarathy, R.; Cripe, P. A.; Groves, J. T. Electrostatically Driven Spatial Patterns in Lipid Membrane Composition. *Phys. Rev. Lett.* **2005**, *95*, 048101.

(39) Sayin, M.; Dahint, R. Formation of Charge-Nanopatterned Templates with Flexible Geometry via Layer by Layer Deposition of Polyelectrolytes for Directed Self-Assembly of Gold Nanoparticles. *Nanotechnology* **2017**, *28*, 135303.

(40) Koklu, A.; Mansoorifar, A.; Beskok, A. Self-Similar Interfacial Impedance of Electrodes in High Conductivity Media. *Anal. Chem.* **2017**, *89*, 12533.

(41) Zhang, P.; Wang, S. Designing Fractal Nanostructured Biointerfaces for Biomedical Applications. *ChemPhysChem* **2014**, *15*, 1550.

(42) Zhou, T.; Ji, X.; Shi, L.; Zhang, X.; Song, Y.; Joo, S. W. AC Dielectrophoretic Deformable Particle-Particle Interactions and Their Relative Motions. *Electrophoresis* **2019**, *00*, 1−7, DOI: 10.1002/elps.201900266.

https://dx.doi.org/10.1021/acs.jpcc.0c00120
J. Phys. Chem. C 2020, 124, 7274−7286

(43) Zhou, T.; Ge, J.; Shi, L.; Fan, J.; Liu, Z.; Woo Joo, S. Dielectrophoretic Choking Phenomenon of a Deformable Particle in a Converging-Diverging Microchannel. *Electrophoresis* **2018**, *39*, 590.
(44) Zhou, T.; Deng, Y.; Zhao, H.; Zhang, X.; Shi, L.; Joo, S. W. The Mechanism of Size-Based Particle Separation by Dielectrophoresis in the Viscoelastic Flows. *J. Fluid Eng.* **2018**, *140*, 091302.
(45) Qian, S.; Ai, Y. Y. *Electrokinetic Particle Transport in Micro-/Nanofluidics*; CRC Press: Boca Raton, 2012.
(46) Polat, M.; Polat, H. Analytical Solution of Poisson-Boltzmann Equation for Interacting Plates of Arbitrary Potentials and Same Sign. *J. Colloid Interface Sci.* **2010**, *341*, 178−185.
(47) Qu, W.; Li, D. A Model for Overlapped EDL Fields. *J. Colloid Interface Sci.* **2000**, *224*, 397−407.
(48) Huang, K.-D.; Yang, R. J. Electrokinetic Behaviour of Overlapped Electric Double Layers in Nanofluidic Channels. *Nanotechnology* **2007**, *18*, 115701.
(49) Ninham, B. W.; Parsegian, V. A. Electrostatic Potential between Surfaces Bearing Ionizable Groups in Ionic Equilibrium with Physiologic Saline Solution. *J. Theor. Biol.* **1971**, *31*, 405.
(50) Shubin, V. E.; Kékicheff, P. Electrical Double Layer Structure Revisited via a Surface Force Apparatus: Mica Interfaces in Lithium Nitrate Solutions. *J. Colloid Interface Sci.* **1993**, *155*, 108.
(51) Chapel, J.-P. Electrolyte Species Dependent Hydration Forces between Silica Surfaces. *Langmuir* **1994**, *10*, 4237.
(52) Dishon, M.; Zohar, O.; Sivan, U. From Repulsion to Attraction and Back to Repulsion: The Effect of NaCl, KCl, and CsCl on the Force between Silica Surfaces in Aqueous Solution. *Langmuir* **2009**, *25*, 2831.
(53) Popa, I.; Sinha, P.; Finessi, M.; Maroni, P.; Papastavrou, G.; Borkovec, M. Importance of Charge Regulation in Attractive Double-Layer Forces between Dissimilar Surfaces. *Phys. Rev. Lett.* **2010**, *104*, 228301.
(54) Nosrati, R.; Hadigol, M.; Raisee, M.; Nourbakhsh, A. Numerical Modeling of Electroosmotic Nanoflows with Overlapped Electric Double Layer. *J. Comput. Theor. Nanosci.* **2012**, *9*, 2228.
(55) Sen, T.; Barisik, M. Size Dependent Surface Charge Properties of Silica Nano-Channels: Double Layer Overlap and Inlet/Outlet Effects. *Phys. Chem. Chem. Phys.* **2018**, *20*, 16719.
(56) Yeh, L.-H.; Xue, S.; Joo, S. W.; Qian, S.; Hsu, J.-P. Field Effect Control of Surface Charge Property and Electroosmotic Flow in Nanofluidics. *J. Phys. Chem. C* **2012**, *116*, 4209−4216.
(57) Hughes, C.; Yeh, L.-H.; Qian, S. Field Effect Modulation of Surface Charge Property and Electroosmotic Flow in a Nanochannel: Stern Layer Effect. *J. Phys. Chem. C* **2013**, *117*, 9322.
(58) Yeh, L.-H.; Zhang, M.; Qian, S. Ion Transport in a PH-Regulated Nanopore. *Anal. Chem.* **2013**, *85*, 7527.
(59) Yeh, L.-H.; Hughes, C.; Zeng, Z.; Qian, S. Tuning Ion Transport and Selectivity by a Salt Gradient in a Charged Nanopore. *Anal. Chem.* **2014**, *86*, 2681.
(60) Ai, Y.; Zhang, M.; Joo, S. W.; Cheney, M. A.; Qian, S. Effects of Electroosmotic Flow on Ionic Current Rectification in Conical Nanopores. *J. Phys. Chem. C* **2010**, *114*, 3883.
(61) Zeng, Z.; Yeh, L.-H.; Zhang, M.; Qian, S. Ion Transport and Selectivity in Biomimetic Nanopores with PH-Tunable Zwitterionic Polyelectrolyte Brushes. *Nanoscale* **2015**, *7*, 17020.
(62) Sen, T.; Barisik, M. Internal Surface Electric Charge Characterization of Mesoporous Silica. *Sci. Rep.* **2019**, *9*, 137.
(63) Sen, T.; Barisik, M. Pore Connectivity Effects on the Internal Surface Electric Charge of Mesoporous Silica. *Colloid Polym. Sci.* **2019**, *297*, 1365.
(64) Atalay, S.; Barisik, M.; Beskok, A.; Qian, S. Surface Charge of a Nanoparticle Interacting with a Flat Substrate. *J. Phys. Chem. C* **2014**, *118*, 10927.
(65) Hill, R. J. Corona Charge Regulation in Nanoparticle Electrophoresis. *Proc. R. Soc. A* **2015**, *471*, 20150522.
(66) Ozcelik, H. G.; Barisik, M. Electric Charge of Nanopatterned Silica Surfaces. *Phys. Chem. Chem. Phys.* **2019**, *21*, 7576.
(67) Ma, Y.; Yeh, L. H.; Qian, S. PH-Regulated Ionic Conductance in a Nanopore. *Electrochem. Commun.* **2014**, *43*, 91.
(68) Yeh, L.-H.; Hsu, J.-P.; Qian, S.; Tseng, S. Counterion Condensation in PH-Regulated Polyelectrolytes. *Electrochem. Commun.* **2012**, *19*, 97.
(69) Yeh, L.-H.; Tai, Y. H.; Wang, N.; Hsu, J. P.; Qian, S. Electrokinetics of PH-Regulated Zwitterionic Polyelectrolyte Nanoparticles. *Nanoscale* **2012**, *4*, 7575.
(70) Brown, M. A.; Arrigoni, M.; Héroguel, F.; Beloqui Redondo, A.; Giordano, L.; Van Bokhoven, J. A.; Pacchioni, G. PH Dependent Electronic and Geometric Structures at the Water-Silica Nanoparticle Interface. *J. Phys. Chem. C* **2014**, *118*, 29007−29016.
(71) Duval, Y.; Mielczarski, J. A.; Pokrovsky, O. S.; Mielczarski, E.; Ehrhardt, J. J. Evidence of the Existence of Three Types of Species at the Quartz-Aqueous Solution Interface at PH 0-10: XPS Surface Group Quantification and Surface Complexation Modeling. *J. Phys. Chem. B* **2002**, *106*, 2937−2945.
(72) Brown, M. A.; Beloqui Redondo, A.; Sterrer, M.; Winter, B.; Pacchioni, G.; Abbas, Z.; Van Bokhoven, J. A. Measure of Surface Potential at the Aqueous-Oxide Nanoparticle Interface by XPS from a Liquid Microjet. *Nano Lett.* **2013**, *13*, 5403−5407.
(73) Davidson, C.; Xuan, X. Effects of Stern Layer Conductance on Electrokinetic Energy Conversion in Nanofluidic Channels. *Electrophoresis* **2008**, *29*, 1125.
(74) Andersen, M. B.; Frey, J.; Pennathur, S.; Bruus, H. Surface-Dependent Chemical Equilibrium Constants and Capacitances for Bare and 3-Cyanopropyldimethylchlorosilane Coated Silica Nanochannels. *J. Colloid Interface Sci.* **2011**, *353*, 301−310.
(75) Hsu, J.-P.; Su, T.-C.; Peng, P. H.; Hsu, S. C.; Zheng, M. J.; Yeh, L. H. Unraveling the Anomalous Surface-Charge-Dependent Osmotic Power Using a Single Funnel-Shaped Nanochannel. *ACS Nano* **2019**, *11*, 13374.
(76) Ma, Y.; Yeh, L. H.; Lin, C. Y.; Mei, L.; Qian, S. PH-Regulated Ionic Conductance in a Nanochannel with Overlapped Electric Double Layers. *Anal. Chem.* **2015**, *87*, 4508.
(77) Yeh, L.-H.; Liu, K. L.; Hsu, J. P. Importance of Ionic Polarization Effect on the Electrophoretic Behavior of Polyelectrolyte Nanoparticles in Aqueous Electrolyte Solutions. *J. Phys. Chem. C* **2012**, *116*, 367.
(78) Brown, M. A.; Abbas, Z.; Kleibert, A.; Green, R. G.; Goel, A.; May, S.; Squires, T. M. Determination of Surface Potential and Electrical Double-Layer Structure at the Aqueous Electrolyte-Nanoparticle Interface. *Phys. Rev. X* **2016**, *6*, 011007.
(79) Karniadakis, G.; Beskok, A.; Aluru, N. *Microflows and Nanoflows*; Springer: New York, 2005.
(80) Li, D. *Electrokinetics in Microfluidics*; Elsevier/Academic Press, 2004.
(81) Veran, S.; Aspa, Y.; Quintard, M. Effective Boundary Conditions for Rough Reactive Walls in Laminar Boundary Layers. *Int. J. Heat Mass Transfer* **2009**, *52*, 3712.
(82) Guo, J.; Veran-Tissoires, S.; Quintard, M. Effective Surface and Boundary Conditions for Heterogeneous Surfaces with Mixed Boundary Conditions. *J. Comput. Phys.* **2016**, *305*, 942.
(83) Achdou, Y.; Pironneau, O.; Valentin, F. Effective Boundary Conditions for Laminar Flows over Periodic Rough Boundaries. *J. Comput. Phys.* **1998**, *147*, 187.
(84) Kosmulski, M. *Surface Charging and Points of Zero Charge*; CRC Press: Boca Raton, 2009.

https://dx.doi.org/10.1021/acs.jpcc.0c00120
J. Phys. Chem. C 2020, 124, 7274−7286